UNIVERSITY OF CALIFORNIA
RIVERSIDE

Modeling and Experimental Studies of Densification Rates in Current Activated Densification

A Thesis submitted in partial satisfaction
of the requirements for the degree of

Masters of Science

in

Mechanical Engineering

by

Alexander Davis Dupuy

June 2011

Dissertation Committee
Dr. Javier Garay, Chairperson
Dr. Guanshui Xu
Dr. Masaru P. Rao

The Thesis of Alexander Davis Dupuy is approved:

_____

_____

_____

Committee Chairperson

University of California, Riverside

ABSTRACT OF THE THESIS

Modeling and Experimental Studies of Densification Rates in
Current Activated Densification

by

Alexander Davis Dupuy
Master of Science, Graduate Program in Mechanical Engineering
University of California, Riverside, June 2011
Dr. Javier Garay, Chairperson

Current Activated Pressure Assisted Densification (CAPAD) has emerged as one of the most promising methods of materials processing in recent years. This process involves the use of large currents to generate heat coupled with applied pressure in what has proven to be a very powerful powder consolidation technique. Despite intensive research, there is still much to learn about the intricacies of how this process works. In the first part of this work, three material systems, yttria stabilized zirconia, Si, and Al, were processed using the CAPAD technique in order to see how processing conditions affect the densification rates in the CAPAD process. It was found that all materials show a peak densification rate at a particular homologous temperature, which is discussed in terms of material bond type. Pressure was found to directly affect the magnitude of the maximum densification rate in all samples. In the second part of this study, a model was developed to estimate the density-temperature relationship in the CAPAD process. This model is dependent on two parameters that are linked to physical quantities. Experimental data for oxide ceramic materials was used to demonstrate the fitting capability of the model. Oxides were chosen because of the abundance of experimental data available in the

literature. Estimating the dominant parameter can be done by finding a material system's activation energy for diffusion and comparing it to other known materials. Guidelines were given on how future CAPAD workers can use the model to save time and resources.

Table of Contents

List of Figures

List of Tables

Chapter 1 - Current Activated Pressure Assisted Densification

1.1 - Motivation

In the realm of materials processing, sintering is one of the most widely applied, intensely researched, and well understood techniques. There even exists a rich history of the process dating back thousands of years. Indeed, the ancients of nearly every continent practiced sintering in some form [1]. Volumes of text could be filled listing all of the applications of sintering as well as the materials systems that have been successfully densified using this technique.

In recent years, Current Activated Pressure Assisted Densification (CAPAD), more commonly known by the trade name SPS^{TM}, has shown promise as a powder consolidation method. Ease of processing and retention of nanocrystallinity are some of the reasons why the CAPAD technique has attracted so much interest. Wide spread use of this technique is restricted by the limited understanding of the finer details of this process. As a result of this, extensive modeling and experimental work has been done to improve the understanding of the CAPAD technique.

The following work is to be divided into two distinctly separate parts. In the first part, the CAPAD process will be examined from a time based performance perspective, namely in the form of a densification rate. Particularly the effects of processing parameters, such as temperature and pressure, as well as material bond type on densification rate will be studied. The second part will present a model of the temperature-density relationship in the CAPAD process based on material and processing parameters. This model is designed with the intent of saving future CAPAD workers both

time and resources by allowing them to more accurately estimate their expected processing temperature.

1.2 - Introduction to powder consolidation

Sintering is the act of consolidating a powder compact into a bulk solid. On a basic level, this occurs due to a driving force in matter to reduce its own surface free energy. At elevated temperatures powder particles that are in contact begin to coalesce as a result of a pressure exerted from this driving force. This pressure drives mass transfer at and around the contact point of the particles (called a neck). Once the particles have come together, the mass transfer continues until most of the porosity has been driven out of the material.

Sintering has a number of advantages over other materials processing techniques. Industrially speaking, sintering is relatively inexpensive, highly scalable, and provides a great degree of reproducibility to manufacturing. Vacuum or gas atmosphere can also be used during sintering to accommodate for the needs of the material system or to provide a precise control of doping. The process is also very robust. Reaction sintering can be performed by physically mixing two powders together rather than using additional chemistry steps. Almost any powder can be consolidated using sintering including nearly all metals, ceramics, and even some polymers. This allows for a diverse range of exotic, as well as common, materials to be processed.

Traditional sintering is not without flaws, however. Processing time can range from hours to days. During this time substantial grain growth occurs in the sample. This extended period of grain growth can lead to pores detaching from the grain boundaries

and becoming trapped within the grains themselves. These locked-in pores are often impossible to get rid of due to the fact that a meaningful reduction in processing time with conventional sintering is not possible. It was this issue that led to the practice, called liquid phase sintering, of adding a small amount of low melting point additive to the desired materials systems. A low melting point additive will melt during processing, enhancing densification and often resulting in full density of the material system. It is important to note that although liquid phase sintering can have a detrimental impact on the properties of the major component; liquid phase sintering is still the most common form of sintering found in industry.

Another remedy for the locked-in porosity issue is through the application of external pressure. Applying an external pressure can confer a number of positive benefits on the densification process. The external pressure can assist the sintering pressure at the neck, adding an extra driving force for mass transport. Particle rearrangement and sliding can also occur, resulting in particles being in a more preferential location for sintering. Lastly, in metals, plastic deformation can occur as a result of the applied pressure, causing increased shrinkage of the sample. These benefits result in reduced processing times and temperatures, thus allowing for higher final densities to be achieved.

1.3 - The CAPAD technique

It can be beneficial to think of the progression of powder densification technology as the pursuit of increased control over processing variables (vacuum sintering controlling atmosphere, Pressure assisted sintering controlling pressure, etc). In light of this, the next logical step for powder processing technology is a finer control of

processing time. Current assisted sintering is one solution to this need. In this process the die is heated directly through joule heating rather than indirectly, as with more traditional methods. The use of a direct heating method allows the sample to reach its densification temperature very rapidly when compared to free sintering.

An example setup schematic of a current assisted process can be seen in Figure 1.1. In a typical current activated method, the die and plungers are usually made of graphite or some other conductive material. These are placed in between two electrodes that are connected to a high current power supply. Pressure is applied by the electrodes for the benefit of the applied pressure as well as to reduce contact resistance. Conductive spacers are typically used to protect the electrodes from the very hot die and plungers.

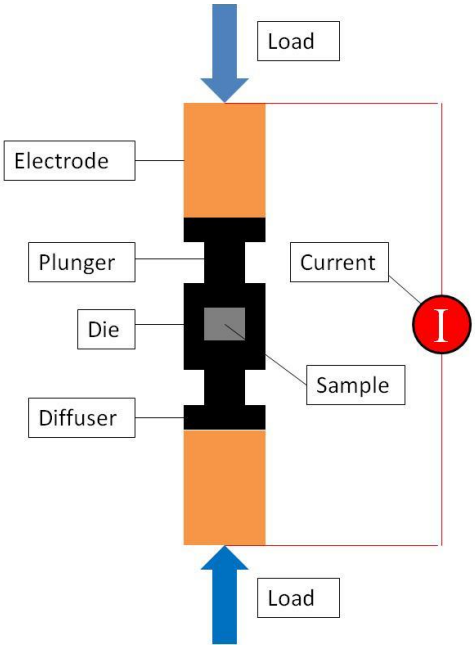

Figure 1.1: Example schematic of current assisted densification device. Points of interest are labeled on the diagram.

Current assisted densification is most commonly known as Spark Plasma Sintering (SPS). This name came about because it was originally theorized that plasma formed in the interparticle space during processing, and this was the reason for SPS's phenomenal capabilities. The presence of sparks and plasma in the SPS process has now been all but disproven under normal operating conditions [2]. Unfortunately, despite being somewhat misleading, the name SPS still appears frequently in literature.

A much more appropriate name for the SPS process is Current Activated Pressure Assisted Densification (CAPAD). In the name CAPAD, the current is correctly emphasized as the dominant driving force in the densification process. Pressure is included in the name because it delivers a non negligible benefit to the densification process, similarly seen in hot pressing. Densification is used as the primary verb in the acronym as opposed to sintering in order to emphasize that sintering is not the only phenomena causing the powder to consolidate. Indeed, the CAPAD technique hosts a variety of possible densification phenomena. Aside from the obvious effects of temperature and pressure described previously, CAPAD can also impart current based enhancements to densification such as electromigration and others [3]. All of these densification effects combined with its rapid heating rate result in a highly efficient densification process that has already been used to process a staggering number of material systems [4].

Most importantly, however, the CAPAD technique gives engineers a more precise control of a material's microstructure than has ever been allowed before. Short processing times allow for the retention of nanocrystallinity. A length scale change in

microstructure can have a substantial effect on a variety of material properties. These include, but are not limited to, mechanical [5], magnetic [6], and ferroelectric properties [7]. Possibly one of the most impressive microstructure-property relationships can be seen with optical materials. Grain sizes smaller than the wavelength of light do not interact significantly with transmitted light. This can lead to transparency in nanocrystalline materials, as has been demonstrated in 8 mol% yttria stabilized zirconia processed with the CAPAD [8].

Successful CAPAD experiments are often the result of precise manipulation of processing parameters. While temperature and pressure are the most commonly thought of processing parameters, the other processing parameters can have a significant effect on the outcome of an experiment. Increased hold time at maximum temperature, for example, is known to increase final densities of samples and is sometimes required when processing certain materials in the CAPAD. Although not studied extensively, an increased pressure application ramp has been shown to increase densification in CAPAD experiments [9]. Faster heating rates are known to theoretically enhance densification [10]. Experimental results, however, offer conflicting results, some showing a positive effect of increased heating rate [11] while others show a negative effect [12]. Control of the cooling rate after an experiment has ended can be beneficial for materials that are susceptible to thermal shock or that go through phase transitions below their processing temperature.

1.4 - Experimental Apparatus

Commercially available CAPAD devices have been available for several years from companies like SPS Syntex. These units are popular among CAPAD researchers due to the difficulty associated with fabricating a CAPAD device in house. For those researches that wish to take advantage of the CAPAD process for its processing efficiency or for the benefits it can confer to many material systems, commercial units are an understandable choice. Unfortunately, commercial units often lack the versatility necessary for more exotic processing requirements. Custom built units are frequently designed with research in mind, often including components of greater accuracy or more advanced data acquisition systems. It is for these reasons that custom built CAPAD units can be better suited for research on the fundamental operation of the CAPAD process.

All of the samples processed in this work were done with a CAPAD device custom fabricated at the University of California, Riverside. Processing occurs in a water cooled high-vacuum chamber (MDC Corp., USA). All samples are performed under a vacuum of $<5x10^{-2}$ torr pulled by a direct drive rotary vane vacuum pump (Alcatel Vacuum Technology, France). Current is provided by three DC power supplies (Xantrex Inc., Canada) which are capable of delivering a maximum of 1200A each.

For all experiments, the powder was packed into a graphite die and contained with two graphite plungers. The inner diameter of the die, and thus the sample diameter, is 19mm. The current is delivered to the die and plungers through two copper electrodes. In this work, temperature is measured using ungrounded type-N thermocouples (Omega Engineering Inc., USA) which are inserted into holes drilled halfway through the die at

its midpoint. Aligning the sample in the middle of the die allows the thermocouple to give the best approximation for the temperature of the sample. Maximum temperature is maintained by using a PID temperature controller (Omega Engineering Inc., USA) which is used to regulate the output of the power supplies.

Load is applied through a universal test frame (Instron Inc., USA) capable of delivering up to 150kN of load. The load frame uses a dual column ballscrew design that gives it a higher degree of precision and control than traditional hydraulic load devices. Test frames like this can very accurately apply and maintain their load, even when the system that the load is being applied to is changing. An extensometer is also built into the device, allowing for the shrinkage of the sample to be accurately tracked.

1.5 - Experimental Procedure

In this work, all CAPAD experiments follow the same basic conditions as outlined in Figure 1.2. This figure shows how the three major processing variables (time, temperature, and pressure) are controlled with respect to one another. For this study, a typical CAPAD experiment will begin with a gradual pressure ramp accompanied by a slow temperature increase (up to ~400°C). After the maximum pressure is reached the temperature ramp begins. Once final temperature has been achieved the sample is held at this temperature for a certain period of time. Finally, when the sample finishes its hold, the system is shut down and the sample is allowed to cool.

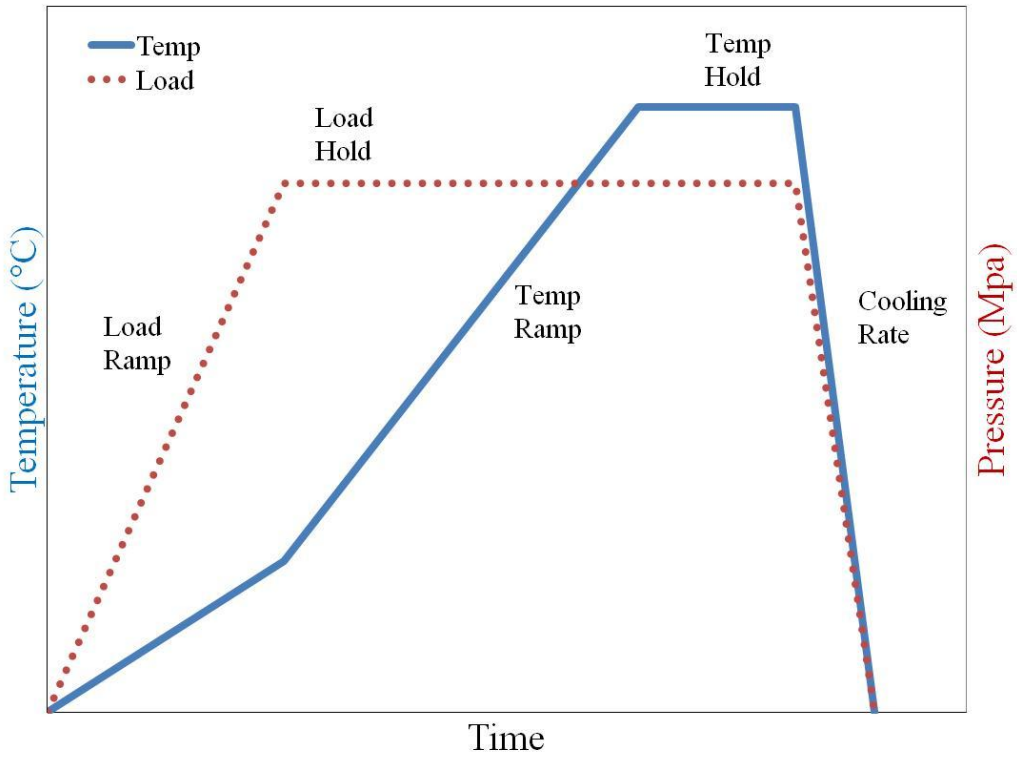

Figure 1.2: Example plots of processing temperature and pressure versus time for a typical CAPAD experiment. The major processing parameters are labeled on the diagram.

As mentioned previously, there are a variety of processing parameters that can be controlled during an experiment. A list of the processing parameters, as well as the values used in this work, can be found in Table 1.1. All samples were processed using the same heating rate, load rate, and hold time at maximum temperature. For all samples, the cooling rate was not controlled. Instead, the current and load were shut off at the end of the experiment.

Table 1.1: List of processing parameters and their values used in this work.

Parameter	Value
Max Temperature (°C)	600-1200
Max Pressure (MPa)	35-106
Heating Rate (°C/min)	200
Load Rate (MPa/min)	35
Temperature Hold (min)	5
Cooling Rate (°C/min)	200-950

Before processing, all samples in this study were cold pressed as powder in the die and plunger set at 71 MPa. This process, called a pre press in this work, is done to give all samples a consistent starting point before processing. Pre pressing ensures that samples have a uniform density before processing. After pre pressing, the starting density, called the green density (ρ_0), is measured geometrically. The green density of a sample varies from material to material depending on that particular material system's sensitivity to deformation and packing.

Chapter 2 - Evaluation of Densification Rates in the CAPAD Technique

2.1 - Introduction

The idea of a densification rate is not new to the CAPAD community. Literature in this field frequently uses the phrase densification rate in discussion. Surprisingly though, there is little experimental data on densification rates in CAPAD. Xu et al [9] examined the effect that load rate has on densification rate in CAPAD. Their findings indicate that densification rate is enhanced with increasing load rate, although the dependence is not one-to-one, but changes with temperature. Langer et al [13] studied densification rates in alumina with both CAPAD and hot pressing. Grain size and pressure effects on densification rates were examined, however this data was used to compare to hot pressing equations. These results showed the similarity in active mechanism between hot pressing and CAPAD.

The goal of this work is to establish the effect that various processing parameters have on densification rates in CAPAD. These processing parameters are temperature and pressure. For this study three different material systems, one for each of the three major bond types, were processed at a variety of pressures and temperatures. Data from the experiments was calibrated so that the true densification rates of the samples could be calculated. From this data, the effect of temperature and pressure on densification rate can be determined.

2.2 - Experimental Procedure

Powders used in this study include 8 mol% yttria stabilized zirconia (8YSZ) (Tosoh Corporation, Japan), Silicon, and Aluminum (Alfa Aesar, USA). Processing conditions for all three materials used in this study are listed in Table 2.1. As indicated in this table, all three powders have a similar grain size and are in the nano regime. This was done to maintain consistency and ensure that powder size related effect would not obscure the final results.

Table 2.1: Summary of the properties and processing conditions of the powders used in this study.

Material	Bond Type	Grain size (nm)	Processing Temp (°C)	Melting Temp (°C)	Processing Pressures (Mpa)	Sample Weight (g)
8YSZ	Ionic	50	1200	2650	35, 71, 106	1
Al	Metallic	70	600	660	71, 88, 106	1.5
Si	Covalent	50	1200	1414	71, 88, 106	1.5

As previously described, the system used in this study is equipped with an extensometer to measure the shrinkage of the sample. Raw data of the extension also includes the results of system compliance. This occurs because of thermal expansion of the graphite parts from the heat that is generated as well as their compression due to the applied load. Calibration is required to remove the effects of system compliance and thus acquire the true shrinkage of the sample. To do this, an empty die and plunger system is processed under the same conditions as the sample it is meant to calibrate. A calibration like this was done for every sample.

Time, displacement, load, and temperature data were collected for each experiment using a 16-Bit data acquisition system with a maximum sampling rate of 250 kHz (National Instruments, TX, USA). With true shrinkage data of the sample it is

possible to determine the in situ density data throughout the experiment. This is done by relating the shrinkage, *l* to the density, ρ by the equation:

$$\rho = \frac{m}{V} = \frac{m}{Ah} = \frac{m}{A(l_0 - l)} \quad (1)$$

where *m* is the mass of the sample, *V* is the volume of the sample, *A* is the cross sectional area of the sample, *h* is the height of the sample, and l_0 is the cold pressed height of the powder compact. The in situ density method was already shown to be accurate in a previous study [9]. Densification rates could be calculated by taking the derivative of a polynomial regression model of the time dependant density data. Noise was filtered using a programmed low pass Butterworth filter.

2.3 - Results

Example in situ density data versus time for all three material systems at 106 MPa of processing pressure can be seen in Figure 2.1. 8YSZ and Si have similar density response over time, beginning with a relatively constant density before 400s and then a rapid rise in density until ~500s where the density remains constant until the experiments are stopped. This behavior implies that a single mechanism dominates the densification process in these materials. Conversely, Al has a much broader densification profile, implying that more than one process contributes significantly to densification. Si has the lowest green density while Al has the highest. It is also worth noting the green densities of the samples are all different. It is likely that Al has a much higher green density due to the fact that the powder is plastically deforming during the pre press.

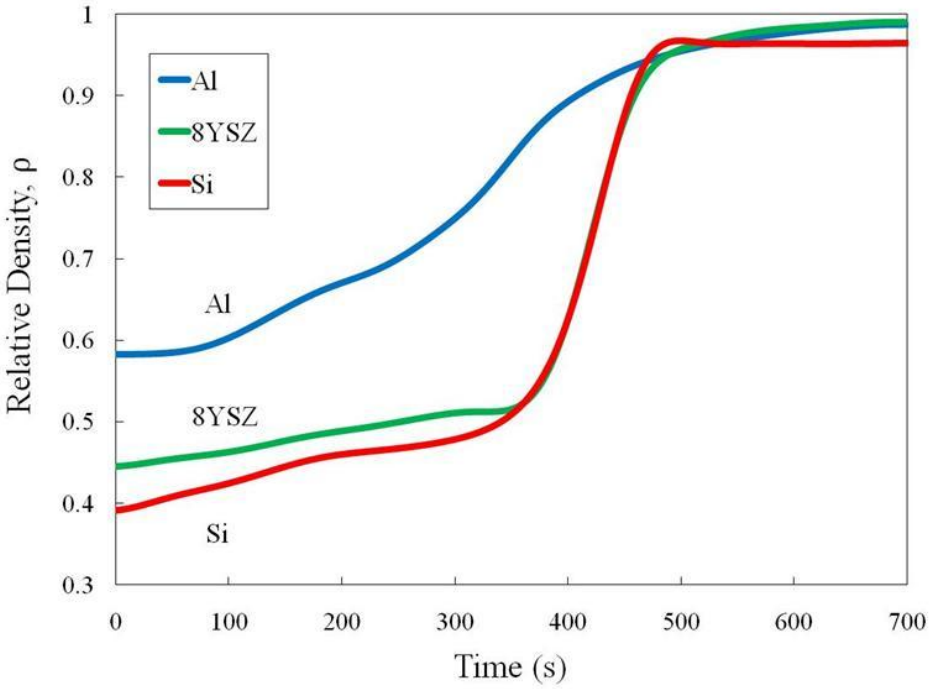

Figure 2.1: Plot of density versus time for the three samples processed at 106 MPa.

Results of densification rate versus homologous temperature for all three materials at 106 MPa of processing pressure can be seen in Figure 2.2. A peak in densification rate can be seen in all three materials. These peaks occur during the sudden change in density seen in processing and represent the primary densification activity during an experiment. Both 8YSZ and Si have a similar densification rate profile as well as densification rate maximum. 8YSZ has a maximum densification rate of 5.2×10^{-3} s^{-1} while Si has a maximum of 5.3×10^{-3} s^{-1}. The greatest difference between the two densification rate profiles is the homologous temperatures at which they occur, with 8YSZ occurring at 0.47 and Si occurring at 0.8. Al has a different behavior from the other two materials, featuring a much lower maximum densification rate and a broader densification rate profile.

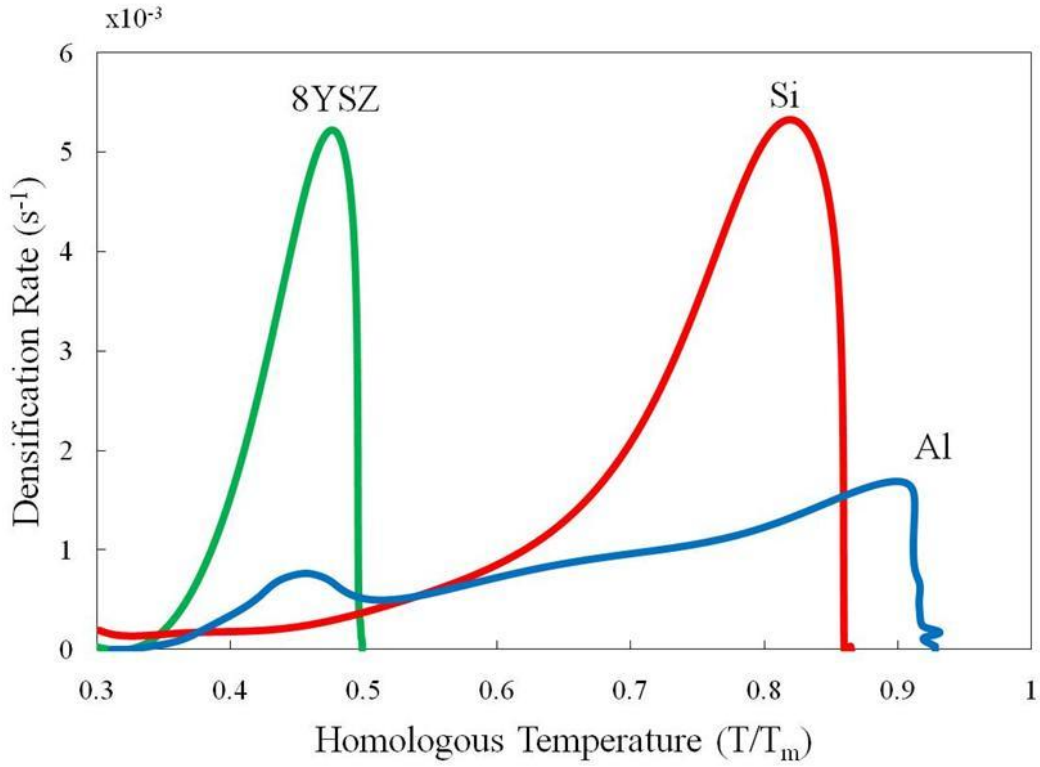

Figure 2.2: Densification rate versus homologous temperature for all three materials at 106 MPa of processing pressure.

Densification rate versus homologous temperature for Al at 106 MPa can be examined more closely in Figure 2.3. The most distinguishing feature of the Al plot is the two densification rate peaks. One peak (the major peak) can be found at a homologous temperature of 0.9 and a densification rate of 1.9×10^{-3} s^{-1}, while the other peak (the minor peak) can be found at 0.45 and 0.76×10^{-3} s^{-1}.

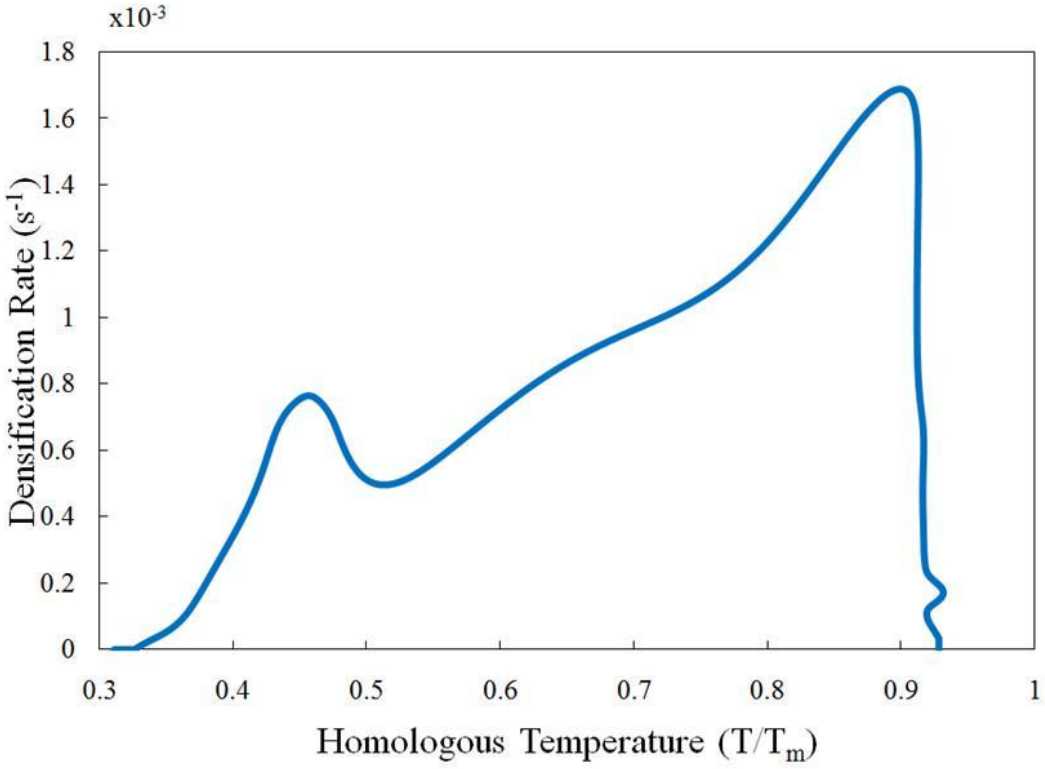

Figure 2.3: Densification rate versus homologous temperature for aluminum processed at 106 MPa

A plot of densification rate versus homologous temperature for all three materials at all processing pressures can be seen in Figure 2.4. Pressure can be seen to have a direct effect on the magnitude of the maximum densification rate peak. In 8YSZ and Si the densification rate maximum increases with increasing pressure. The change in magnitude with pressure is not the same for both materials. Si clearly shows a greater change in densification rate with pressure than 8YSZ does. Al again shows an unusual trend, with increased pressure decreasing the densification rate at the major peak.

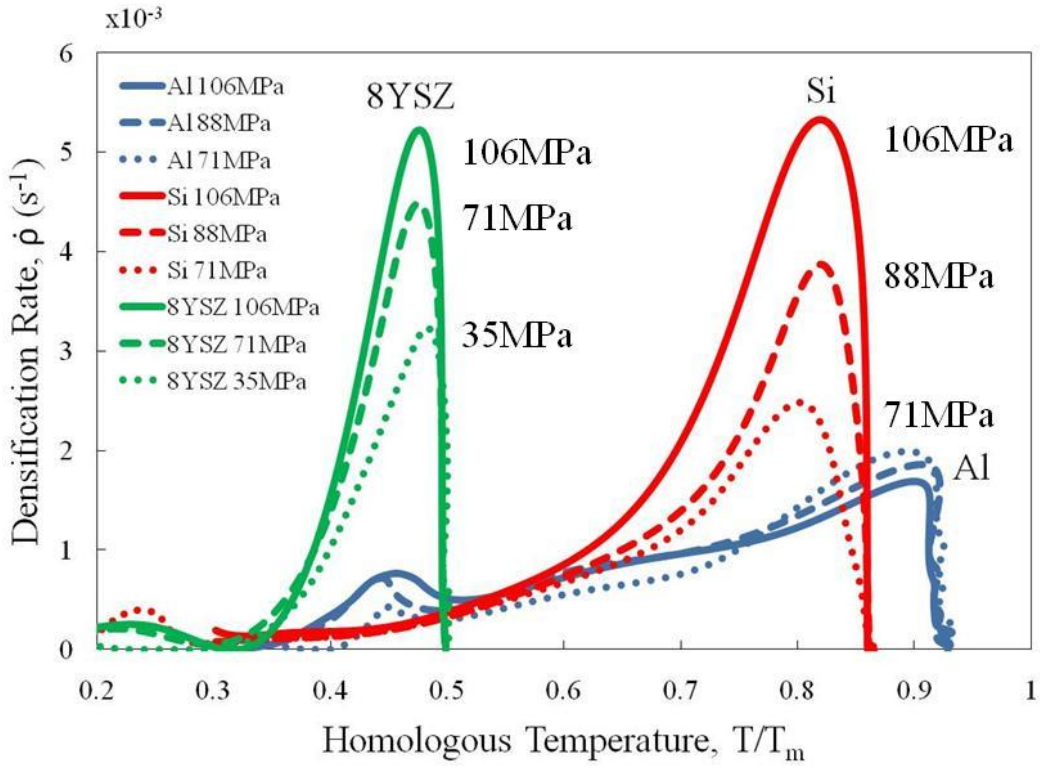

Figure 2.4: Densification rate versus homologous temperature for all three materials at all processing pressures.

Densification rate versus homologous temperature for Al at all processing pressures can be examined more closely in Figure 2.5. A change in pressure affects the two densification rate peaks differently in Al. At the minor peak an increase in pressure produces the expected result of increasing the densification rate. Conversely, the opposite trend occurs at the major peak.

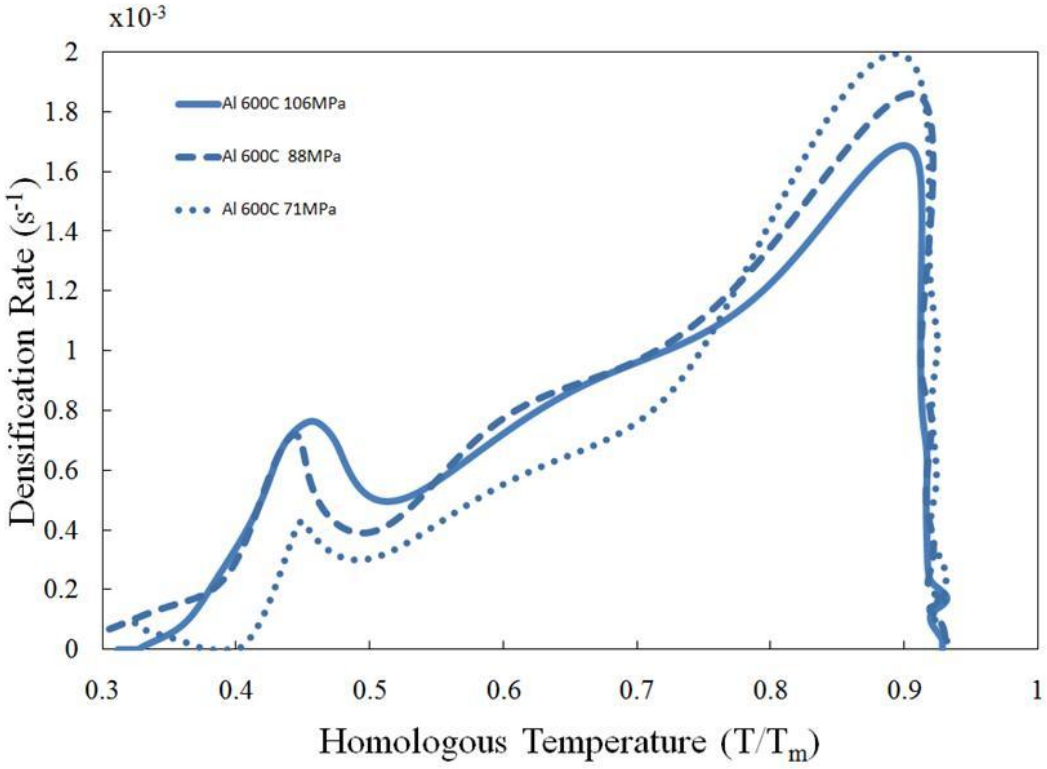

Figure 2.5: Plot of densification rate versus homologous temperature for Al at all processing pressures

2.4 - Discussion

All three materials have peak densification rate positions that correspond well with previously identified trends [14]. Typically, ionic materials require the lowest homologous temperature to process while metals require the greatest, with covalently bonded materials in the middle. Such generalities may not always be sufficient to justify reported data, however. For example, a more meaningful justification for why Si requires a greater homologous temperature than 8YSZ can be seen by examining the activation energy for volume diffusion (Q_{vol}) for these two materials. By normalizing the activation

energy by melting temperature (Q_{vol}/RT_m), where R is the gas constant, it can be seen that Si (27-34) [15] has a higher activation energy than 8YSZ (19) [16].

For 8YSZ and Si, the effect of pressure on maximum densification rate is logical in light of what is understood about pressure effects in hot pressing. Pressure increases diffusion kinetics as well as influencing more mechanically inclined densification mechanisms. The two peaks in Al having a different densification rate trend is not immediately obvious, however. A likely explanation for the presence of the minor peak is that it is related to temperature dependant plastic deformation, as creep is known to be present in nanocrystalline Al at that temperature and under those pressures [17]. This also explains the response to pressure seen at the minor peak. Increased pressure will directly increase the degree of plastic deformation at all temperatures. The major peak is likely a product of the more commonly seen densification phenomena, such as sintering, found in the other two materials. At the major peak the inverse trend with pressure can be explained as a saturation effect from the minor peak. Greater pressures result in greater densification at the minor peak, leaving less density to be achieved at the major peak.

A qualitative look at Figure 2.4 indicates that Si has the greatest response to applied pressure. This can be seen more clearly in Figure 2.6, which is a plot of maximum densification rate versus pressure for 8YSZ, Si, and both peaks of Al. From this data it is possible to extract pressure sensitivity by calculating the slope of the line. As originally observed, Si has the highest pressure sensitivity with 8.05×10^{-5} MPa^{-1} s^{-1} while 8YSZ comes in second with a pressure sensitivity of 2.82×10^{-5} MPa^{-1} s^{-1}. Al has the lowest sensitivities, with the minor peak being equal to 0.95×10^{-5} MPa^{-1} s^{-1} and the

absolute value of the major peak being equal to 0.87 x 10^{-5} MPa^{-1} s^{-1}. Both the major and minor peaks possess pressure sensitivities that are very similar. In light of the fact that the two peaks represent two different physical phenomena, this result should not occur.

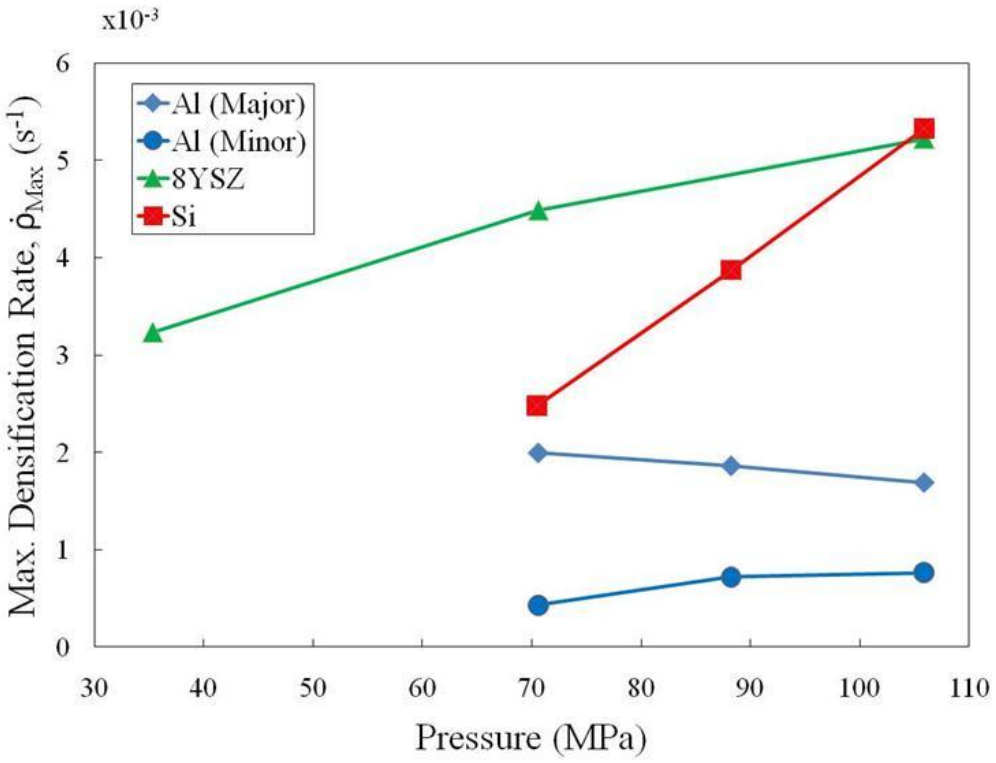

Figure 2.6: Plot of maximum densification rate versus pressure for all three materials

Another way to visualize pressure sensitivity can be seen in Figure 2.7, which is a plot of change in maximum densification rate normalized to the maximum densification rate at 106 MPa versus processing pressure. From this figure it can be seen that Si again has the greatest response to pressure, but now Al can be seen to be more sensitive to pressure than 8YSZ. One possible explanation for these results can be found by thinking about the difference between the nominal applied pressure and the actual pressure achieved during processing. It is known that thermal expansion during processing can

produce stress gradients in CAPAD [18]. If a material has a thermal expansion coefficient that is different from the coefficient for graphite, then non negligible stress gradients can form during processing. It is known that 8YSZ has a thermal expansion coefficient that is similar to graphite, and thus will not produce an appreciable stress gradient. Al and Si, on the other hand, have very different coefficients from graphite, and as a result may have an actual pressure that is higher than in the 8YSZ samples.

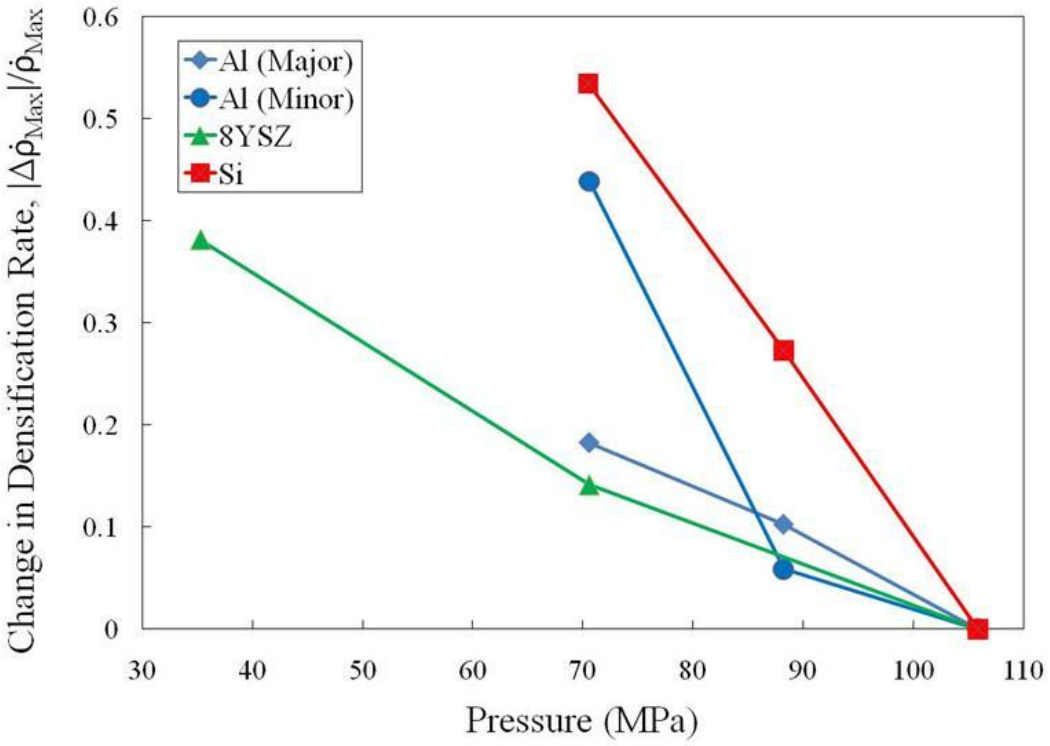

Figure 2.7: Plot of the change in maximum densification rate normalized to the densification rate at 106 MPa versus pressure for all three materials

It should also be possible to explain the effect of pressure on densification rate by examining the effect that pressure has on diffusion. For example, Antonelli et al [19] studied the effect that pressure has on the activation energy for diffusion in Si. Their

work indicates that pressures over an order of magnitude greater than the pressures applied in this study are necessary to affect the activation energy in a meaningful way. Within the pressure ranges in this study, it is unlikely that the activation energy for diffusion is directly affected.

Pressure is also known to affect mass transfer by altering the driving force for diffusion [20]. An applied pressure creates a potential field g on a particle. The gradient of this field describes the force on this particle that influences mass transfer. This force, along with concentration gradient, drives atomic flux J in the form of:

$$J = -D\nabla c - \frac{Dc\nabla g}{kT} \quad (2)$$

where, c is the concentration of the diffusing species, D is diffusivity, k is Boltzmann's constant, and T is temperature. In equation (2), the first term on the right hand side is the flux due to concentration gradient, or Fick's first law. The second term is the flux due to the stress induced potential field.

Looking specifically at the second term, it can be seen that the applied pressure will have the greatest impact on the material with the larger diffusivity. A list of the diffusivity data at the processing temperatures used in this study can be found in Table 2.2. 8YSZ can be seen to have the lowest diffusivity, which matches well with the results of this study. Diffusion data for Al and Si, however, imply a different behavior than what is found experimentally. According to the data, Al should be more greatly influenced by pressure than Si. This trend is reversed in the experimental data. It is worth noting, however, that the Al started with a higher green density than the other two materials,

thereby having less densification left to achieve during processing. The higher green density can therefore mask the true behavior of the Al.

Table 2.2: List of diffusion data for the materials processed in this study at the listed temperatures. Data is from the following references 8YSZ [16], Si [21], and Al [22].

Material	Q (kJ/mol)	D_0 (cm^2/s)	Processing Temp (K)	D (cm^2/s)
8YSZ	460	0.22	1473	1.07E-17
Si	495	9000	1473	2.52E-14
Al	120.5	0.035	873	2.16E-09

It can now be seen from Figure 2.7 that the major and minor peaks in Al no longer have the same pressure response. While the major peak appears to be linear, the minor peak does not. At 71MPa of pressure there is an abrupt change in the pressure response compared with the change that occurs at 88 MPa. This sudden shift potentially indicates a change in mechanism, possibly a change to another creep mechanism. To verify this, it is necessary to look at the grain size dependant deformation maps for Al seen in reference [17]. Based on the starting powder (70 nm grain size) the grain size normalized to the burgers vector for Al would be 245. At the given processing pressures, the data is likely right on the cusp of the power law creep-Coble creep transition. At 71 MPa of pressure the dominant creep mechanism may still be coble creep, but the additional pressure could put the deformation into power law creep. Alternatively, as described in the reference, pressures higher than our nominal pressure causes the traditional creep equations to break down, resulting in creep rates that increase rapidly with pressure. This could explain the observed behavior if it is remembered that the true stress values during processing are likely higher than those reported.

2.5 - Conclusions

CAPAD experiments were performed on nanocrystalline 8YSZ, Si, and Al in order to address the effect that processing parameters have on densification rates. Processing parameters examined include applied pressure, processing temperature, and material bond type. To find the true densification rates of the samples, a method was described to eliminate the effects of system compliance through calibration and to calculate the densification rates from the raw data. In all samples processed it was found that there is a peak value of densification rate that occurs at a particular homologous temperature that varies from material to material. Al was found to have two densification rate peaks, corresponding to two different densification mechanisms. Pressure was found to directly change the magnitude of the densification rate for all materials. With this data it was possible to examine the relative sensitivity to pressure of each material.

Chapter 3 - Empirical Modeling of the Density-Temperature Relationship in CAPAD

3.1 - Introduction

Many plots of relative density (ρ) versus processing temperature for a material processed with the CAPAD technique show a clear sigmoidal relationship. This relationship is an outcome of the physical phenomena involved in densification. Low values of the materials homologous temperature (T/T_m) result in an asymptotic constant density. This value is called the green density (ρ_0), and is dependent on sample preparation and applied pressure. At a certain T/T_m (depending on the material), the density function adopts an exponential relationship with T/T_m. Here the material begins to overcome its activation energy for diffusion, allowing for a significant amount of densification. After this, the plot adopts a linear appearance and the tangent of the line, or the densification rate ($\dot{\rho}$), reaches its maximum value. The homologous temperature that this corresponds to is denoted as "a" in this work. Finally, the density function begins to saturate, resulting in a logarithmic response followed by an asymptotic approach towards 100% relative density.

In a recent review paper [14] Garay highlighted the effect that T/T_m has on CAPAD densification behavior. Figure 4 of the review shows ρ *vs* T/T_m for a variety of materials. Most of the data is sigmoidal. What data is not sigmoidal is likely due to a low density (i.e. MgO, TiO_2, and SiC) or there being different mechanisms involved in densification (i.e. all of the metals). None the less, the figure illustrates the wide diversity

in density-temperature relationships across material type as well as the diversity in *a* value amongst different materials.

Garay[14] further goes on to describe the characteristics of the density function by examining the slope of the line. This slope is denoted as *s* and is defined as the temperature sensitivity of the material. The *s* value fits into a simple linear fit relationship of the form,

$$\rho = s\left(\frac{T}{T_m}\right) + b \tag{3}$$

where b is the intercept on the density axis. While this equation does not define a sigmoidal function, it does allow some physical properties (namely *a*, *s*, and *b*) to be examined across different material classes. In this work, an empirical model will be developed around these parameters in order to provide researchers with rough guidelines when they embark on future CAPAD experiments. Oxide ceramics will be examined exclusively in this work due to the abundance of experimental data available in literature.

3.2 - Previous Modeling of Powder Consolidation Techniques

Models for traditional sintering were discovered through a combined effort of experimental and theoretical pursuits. Equations for the stages of sintering were formulated by Coble [23]. These equations are based on the behavior of grains during processing, whose geometric changes are used to represent the overall geometric change during the sintering process. Each stage of sintering is represented by a different structure that is used to formulate the equations for that particular stage. The first stage of sintering is represented by a two particle system in close contact that has begun to form a neck.

Both the second and third stages are modeled after a truncated octahedron, representing a grain, with different pore structures.

Equations for hot pressing were also formulated by Coble [24]. In this model, the first and third stages of sintering are modeled using the same equations as the traditional sintering model except for a change in the driving force terms. While the original sintering equations used a driving force term that depended only on the surface energy of the material, the hot pressing equations must account for the applied pressure as well. The second stage of sintering in hot pressing was formulated by adapting existing creep models.

Through models like the ones created by Coble, it became possible to achieve a greater understanding of the sintering process and to better estimate the outcome of experiments. One example of this was the idea of sintering diagrams developed by Ashby [25]. Sintering diagrams are plots of particle neck radius versus homologous temperature. These diagrams indicate sintering behavior for individual materials. They are constructed by equating the rate equations for each sintering mechanism. Regions based on dominant mechanism are defined on the diagrams. Contours of neck growth time and sintering rate are also included. It is through diagrams like these that researchers can better understand the sintering behavior of the material system that they are working on.

Further efforts to estimate the outcome of sintering experiments resulted in the development of the Master Sintering Curve (MSC) [26]. A MSC is a plot of density versus thermal history for a material being sintered under specific processing conditions. By constructing isothermal or constant heating rate curves, the effect of varying the

heating rate and processing temperature, respectively, can be examined. To construct these plots, it is necessary to use existing data points to estimate the activation energy for sintering. The calculations for a MSC assume dominance of one type of diffusion mechanism during sintering, and thus are not suitable for every material system.

Due to its complexity, the CAPAD process has yet to be fully modeled. While a complete model of the CAPAD process has not yet been discovered, there have been numerous examples of limited modeling being used to further the understanding of the CAPAD process as well as to estimate processing outcomes. Both analytical and numerical modeling have been found to be viable options for use in CAPAD modeling. Olevsky et al [27], for example, constructed a model for analyzing the importance of thermal diffusion in the CAPAD process.

The difficulty in modeling the CAPAD process has necessitated the use of alternative modeling strategies. One such strategy was proposed by Maizza et al [28]. This strategy involved using actual CAPAD experiments to help estimate constants used in a finite element model. Their self-refining model could then be used to estimate the results of future CAPAD experiments. On a similar line of thinking, Guillon et al [29] recently identified a method for constructing a MSC for the CAPAD process. These strategies demonstrate the exciting possibilities that lie ahead for those in the CAPAD community.

3.3 - Procedure

3.3.A - Model Development

Sigmoidal functions are well known to engineers and scientists, with one of the most prevalent example being the Fermi function,

$$f(E) = \frac{1}{exp\left(\frac{E - E_F}{kT}\right) + 1} \tag{4}$$

where f(E) is the probability that an electron is at the energy level E, E_F is the Fermi energy, and k is Boltzmann's constant. Equation 4 results in a sigmoidal function describing a probability ranging from 0 to 1. It should be possible to construct an equation that approximates the sigmoidal density-temperature relationship.

Using the sigmoidal form as a starting point, the density function can be expressed as,

$$\rho = \frac{1}{exp\left(-\frac{(T/T_m) - a}{0.1/s}\right) + 1} = tanh\left(\frac{(T/T_m) - a}{0.2/s}\right) \tag{5}$$

In order to make the *s* parameter meaningful for this model, it is necessary to use a different definition than is used in the review by Garay [14]. Here the slope of the linear section of the line is used, rather than using the slope of the entire density line. Equation 5 results in a sigmoidal function that has a lower bound at T/T_m =0 with ρ=0 and an upper bound at T/T_m =1 with ρ=1. This is not physically correct due to the fact that all powder samples posses a non zero density after being loaded into their die.

To make this model account for the experimental data, equation 5 must compensate for green density by shifting the bottom asymptote up to the value of ρ_0. This can be done by modifying equation 5 to,

$$\rho = \frac{1}{1+z}\left(\frac{1}{exp\left(-\frac{\left(\frac{T}{T_m}\right)-a}{\frac{0.1}{s}}\right)+1}+z\right) \qquad (6)$$

$$\rho = \left(1+z+tanh\left(\frac{(T/T_m)-a}{0.2/s}\right)\right)\frac{1}{2+z}$$

where z is the green density shifting term. While z is not the green density itself, it is dependent on ρ_0. The z term can be found by setting T/T_m =0 and $\rho = \rho_0$ and solving for z. This gives the equation,

$$z = \frac{1}{\rho_0 - 1}\left(\frac{1}{exp\left(\frac{a}{0.1/s}\right)+1}-\rho_0\right) = \frac{tanh\left(\frac{-a}{0.2/s}\right)+1-2\rho_0}{\rho_0-1} \qquad (7)$$

Using these two equations, it is possible to approximate the final density of a CAPAD experiment with respect to the processing temperature. This analysis requires that the physical parameters a, s, and ρ_0 be known. These values can be determined if sufficient data for the material system is available. The a value can be determined by examining the raw data from the experiment while the s value can be found from measuring the slope of the straight line segment of the ρ *vs* T/T_m plot. It should be noted that both the a and s parameter are dependent on the properties of the material as well as

the processing parameters of the sample. Different values for the parameters will be achieved under different processing conditions, even if the material being processed is the same.

If sufficient data is not known then it is necessary to back out the parameters using what data is available. By using numerical methods and a minimum of two known data points, it is possible to solve equation 6 simultaneously to acquire the unknown parameters. If two parameters are unknown (i.e. a and s), then a minimum of two data points are required to produce the unknown parameters. Three data points are required if all of the parameters are unknown. While it is possible to solve the parameters using only the minimum number of data points, having excess data points will improve the accuracy of the results. A method like this can be very useful owing to the fact that most studies consider values of ρ<95% to be undesirable and thus do not report them in the literature. This scenario is seen very often and makes the slope calculation of s impossible due to the fact that the straight line segment often occurs at values of ρ<90%.

3.3.B - Experimental Procedure

Standard CAPAD operating procedure for this study was outlined in the first chapter. To test the validity of this model in a practical scenario, it was decided to process an unfamiliar material system. Briefly, commercially available Strontium Titanate (STO) (Inframet Advanced Materials) was used with a grain size of 100 nm. Samples were processed using 1.5 g of powder, 106 MPa of pressure, a 200 °C/min heating rate, and a dwell time at temperature of 5 minutes. Final temperatures used were 830°C (T/T_m =0.47) and 900°C (T/T_m =0.5) and final densities were measured using the Archimedes method.

3.4 - Results

Figure 3.1 demonstrates the effect of varying the *a* value on the density function assuming a constant *s* and ρ_0 value of 3 and 0.5 respectively. Each curve represents a different value of *a*. Increasing the *a* parameter has the effect of shifting the entire density plot over to the right, dramatically changing the expected density at all temperatures. Likewise, Figure 3.2 shows the effect of varying the *s* value assuming a constant *a* and ρ_0 of 0.5 for both. All of the curves are pinned at the *a* value. As the *s* parameter is increased the density function becomes steeper, signifying a greater achievable densification from less temperature.

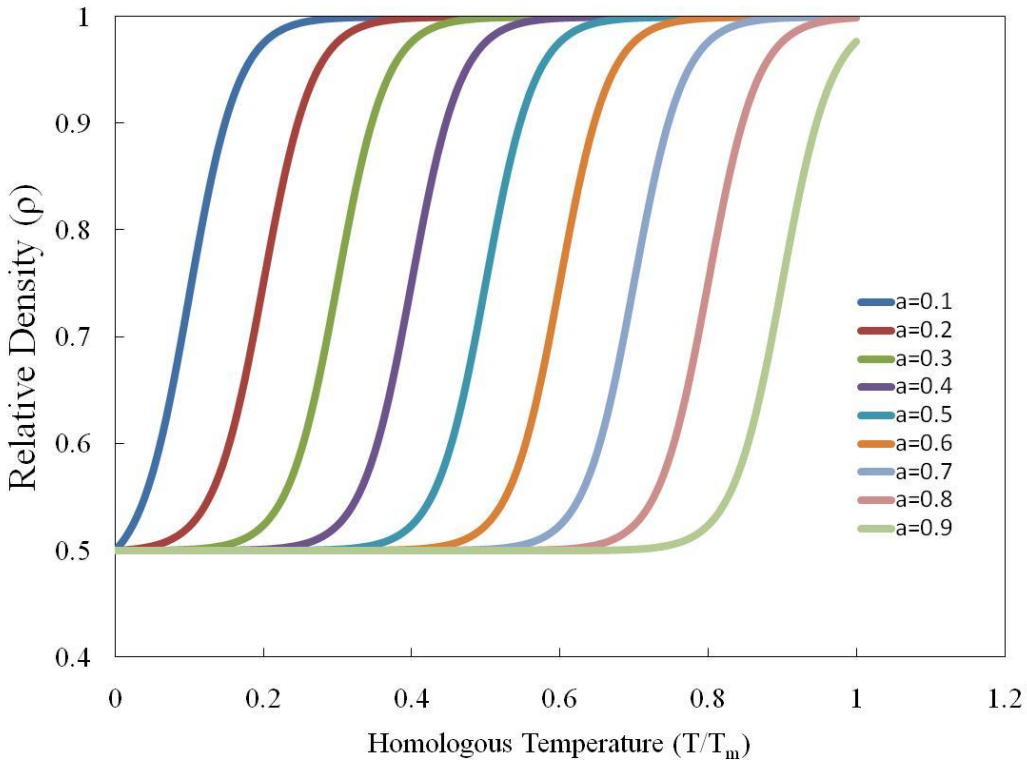

Figure 3.1: Plot of relative density versus homologous temperature if *s* is held constant but *a* is varied

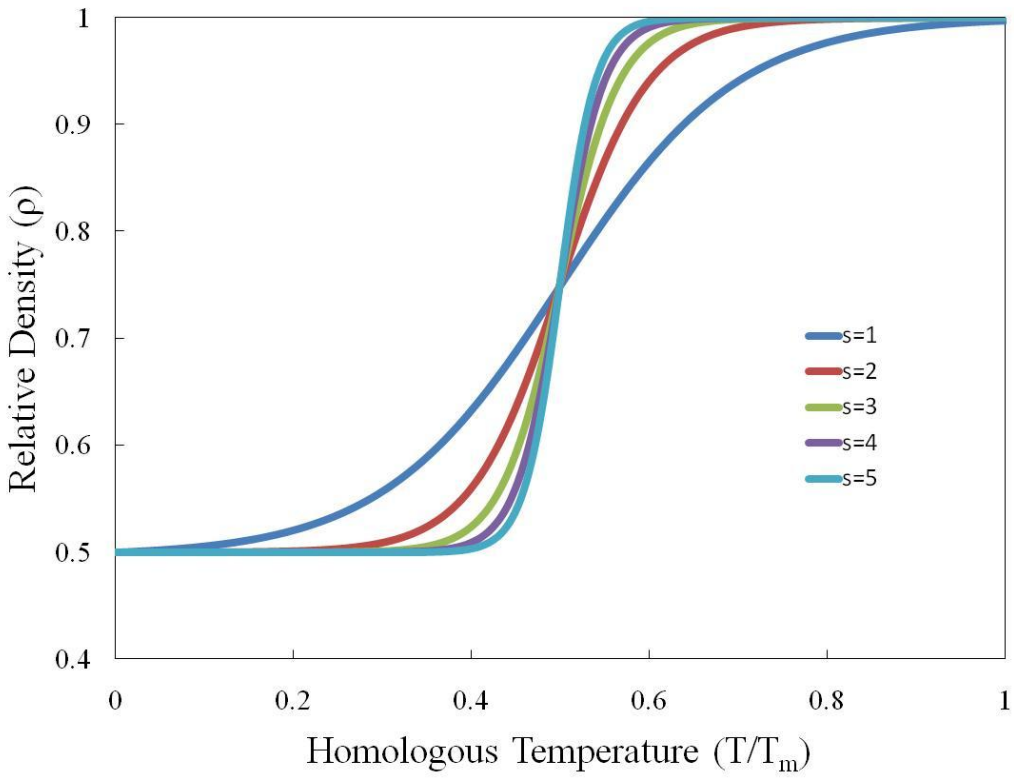

Figure 3.2: Plot of relative density versus homologous temperature when *a* is held constant and *s* is varied

To demonstrate the effectiveness of the equation, data of 8 mol% yttria stabilized zirconia (8YSZ) [30] and Al_2O_3 [11] were fit to the equation 6. These materials were chosen because they are two of the most well researched oxide materials. Figure 3.3 depicts the calculated values from equation 6 as well as the experimental data for the 8YSZ and the Al_2O_3. The fitting parameters for these data sets, as well as the other data sets used in this study, are shown in Table 3.1. It can be seen from the 8YSZ data that the *a* parameter decreases while the *s* and ρ_0 parameters increase with increasing pressure. Interestingly, the *s* parameter for 8YSZ and Al_2O_3 are very similar. This similarity does not hold for the *a* parameter, which differs substantially from 8YSZ. Data for the STO

samples can also be found in Table 3.1. Final densities for the STO samples were ρ=0.57 at T/T_m=0.47 and ρ=0.68 at T/T_m=0.5. STO possesses an *a*=0.51 and a *s*=3.

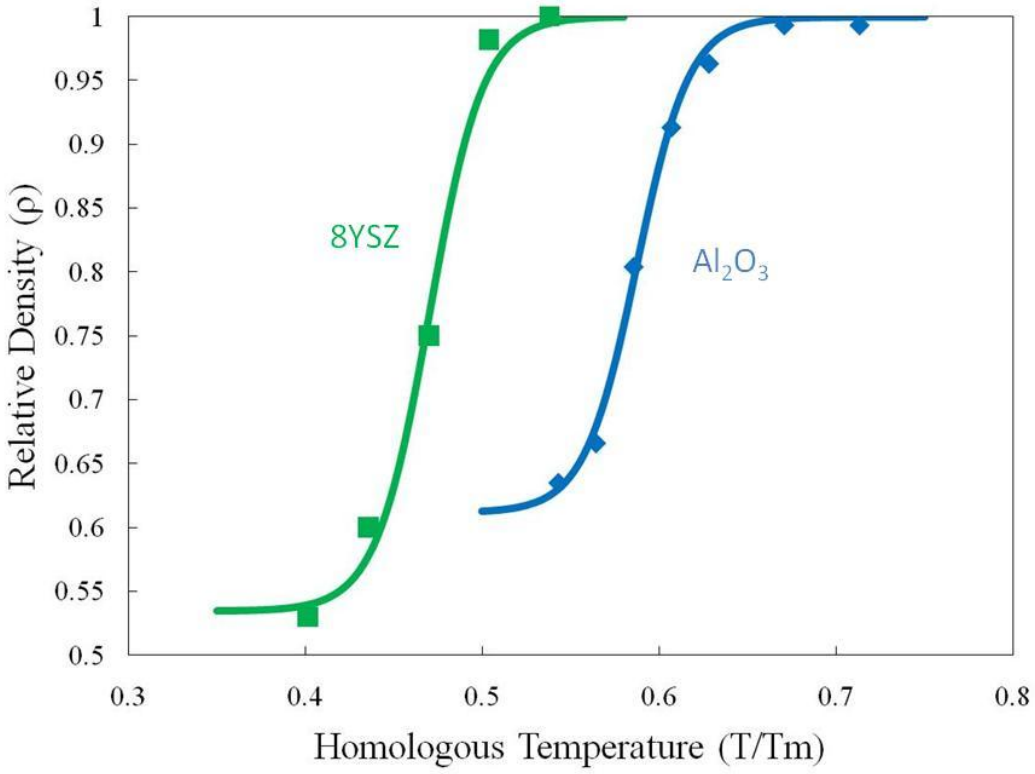

Figure 3.3: Plot of relative density versus homologous temperature for 8YSZ and Al_2O_3. The data points are from actual experimental data while the lines represent the modeled data. Experimental data is from: 8YSZ [30] and Al_2O_3 [11].

Table 3.1: List of model parameters for all four data sets used in this study as well as their activation energy for grain boundary diffusion normalized by melting temperature. The activation energies are from the following references: 8YSZ [16], Al_2O_3 [31], TiO_2 [32], and STO [33].

Material	a	s	ρ_0	Q/RT_m
8YSZ	0.4701	6.6035	0.5346	12.7
Al203	0.5875	6.7529	0.6114	28-45
TiO2	0.525	3.174	0.45	14.5-18
STO	0.51	3	0.45	24

3.5 - Discussion

3.5.A - Fitting of Experimental Data

Figure 3.3 demonstrates that equation 6 is capable of fitting a density temperature relationship for a CAPAD experiment well enough that it could be used to estimate the results of future CAPAD experiments. As demonstrated from this work and the review from Garay [14], material systems can vary widely in their CAPAD processing requirements. Knowing the proper values for the parameters *a* and *s* is critical for this model to work. These parameters will need to be estimated if previous data for a material system is not available.

For this purpose, the data from 8YSZ and Al_2O_3 can be used as bounds on the range for the *a* parameter. 8YSZ and Al_2O_3 represent relatively ideal candidates for their respective bond types. The nature of the bonding in the material being processed should indicate which bound the *a* value should be closer too. To test this assumption, data from a CAPAD study of TiO_2 [34] was used for comparison. Data from this study gives TiO_2 the parameters of approximately a=0.525 and s=3.175. Compared to the values for 8YSZ and Al_2O_3, TiO_2 has an *a* parameter that is exactly halfway between the two bounds and a *s* parameter that is roughly half as much as the two bounding materials. From the perspective of the bond type bounding guidelines this does not make any sense, as the parameters for TiO_2 should tend towards the parameters for 8YSZ.

The error associated with selecting an incorrect *s* parameter for TiO_2 can be seen in Figure 3.4Figure 3.4: Plot of the error between the model and experimental data points versus *s* parameter assuming the *a* parameter is constant. The experimental density is

labeled beside the line it corresponds to.. In this plot the y axis corresponds to the error between the model and the experimental data while the x axis corresponds to the *s* parameter. Each line corresponds to a different experimental data point. The *a* parameter is held constant at 0.525 and the calculated density is compared to the density of the three known data points at their respective temperatures. From this figure we can see that the *s* parameter is relatively forgiving. Even if an *s* parameter of 6.6, the value for 8YSZ, is chosen the absolute error in density would only be about 7%.

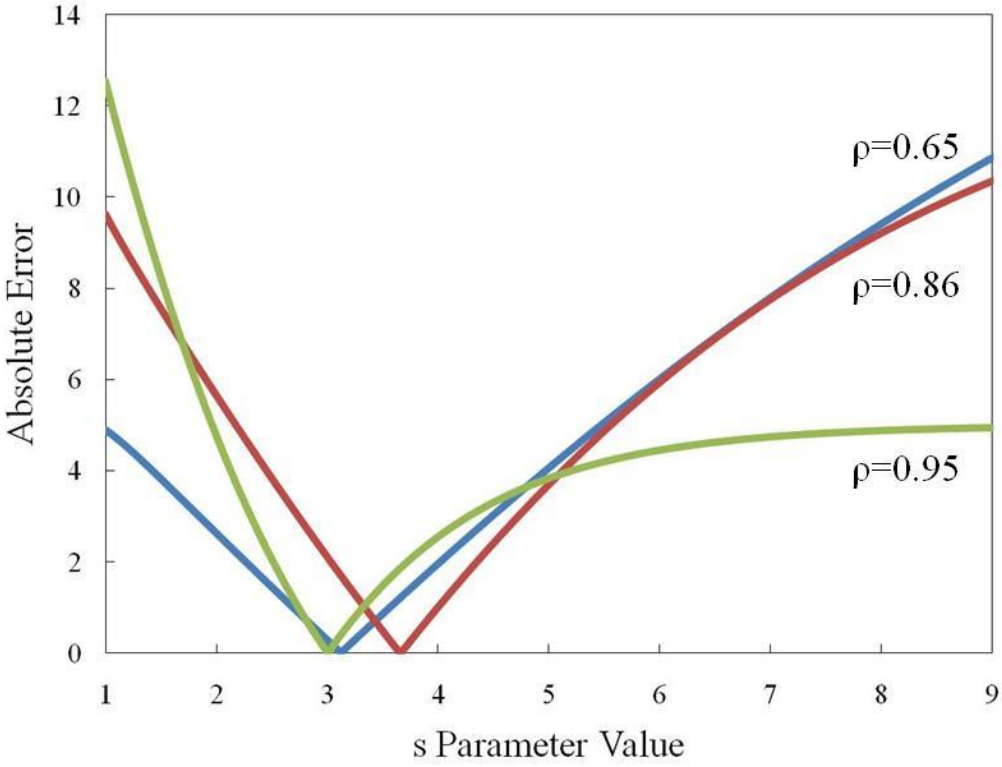

Figure 3.4: Plot of the error between the model and experimental data points versus *s* parameter assuming the *a* parameter is constant. The experimental density is labeled beside the line it corresponds to.

Similarly, the error analysis for the *a* parameter in TiO_2 can be seen in Figure 3.5. It can be seen that, unlike the *s* parameter, the penalty for selecting an incorrect *a*

parameter is very high. If the *a* parameter for 8YSZ or Al_2O_3 were selected the error in TiO_2 would be greater than 20%. This indicates that a proper estimation of the *a* parameter is critical for the model to be useful.

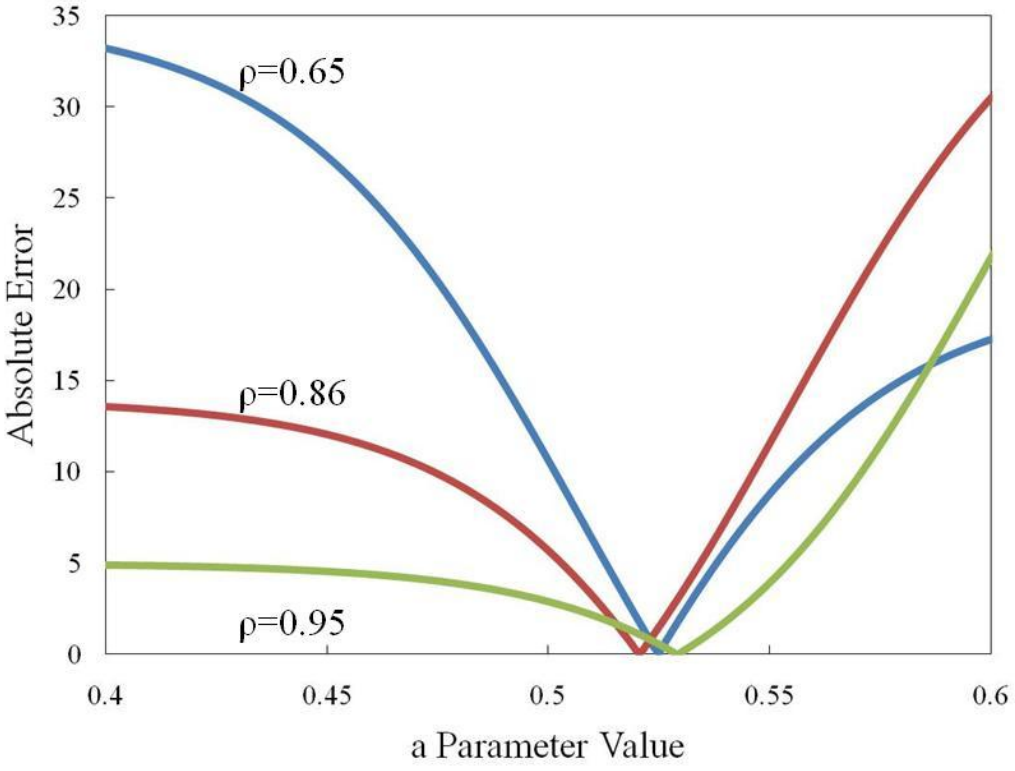

Figure 3.5: Plot of the error between the model and experimental data points versus *a* parameter assuming the *s* parameter is constant. The experimental density is labeled beside the line it corresponds to.

Much like TiO_2, STO also does not fall in line with the bond based bounding guidelines. Parameters for STO are more similar to TiO_2 than to any other material examined here. In both examples from literature and an experimental study, bond based parameter estimations have failed to produce parameter values that are within an acceptable error. Since proper estimation of the *a* parameter is required for the model to be useable, it is necessary to find another method of estimating parameters.

Densification during the CAPAD process is predominantly controlled by diffusion. It should therefore be possible to cast the *a* parameter in terms of mass transfer principles. When a material begins to densify appreciably, it is because the system has acquired enough thermal energy to overcome its own activation energy for diffusion. Thus, even the *a* parameter itself can be thought of as representing a thermal energy required to reach maximum densification.

In light of this, the *a* parameter should have some correlation to activation energy for diffusion. Table 3.1 contains the activation energy normalized to melting temperature for all four materials. A range of activation energy is provided when the literature data is contradictory. Figure 3.6 shows a plot of normalized activation energy versus *a* parameter for all four materials. The dashed line is a best fit line to emphasize the trend. It can be seen that STO and TiO_2 fall in between 8YSZ and Al_2O_3 in terms of *a* parameter as well in terms of normalized activation energy. The lack of perfect linearity in the figure could be due to the differing processing parameters between the data sets. There is some variation in applied pressure, grain size, and hold time amongst the data sets. This could lead to some offset in the *a* parameter.

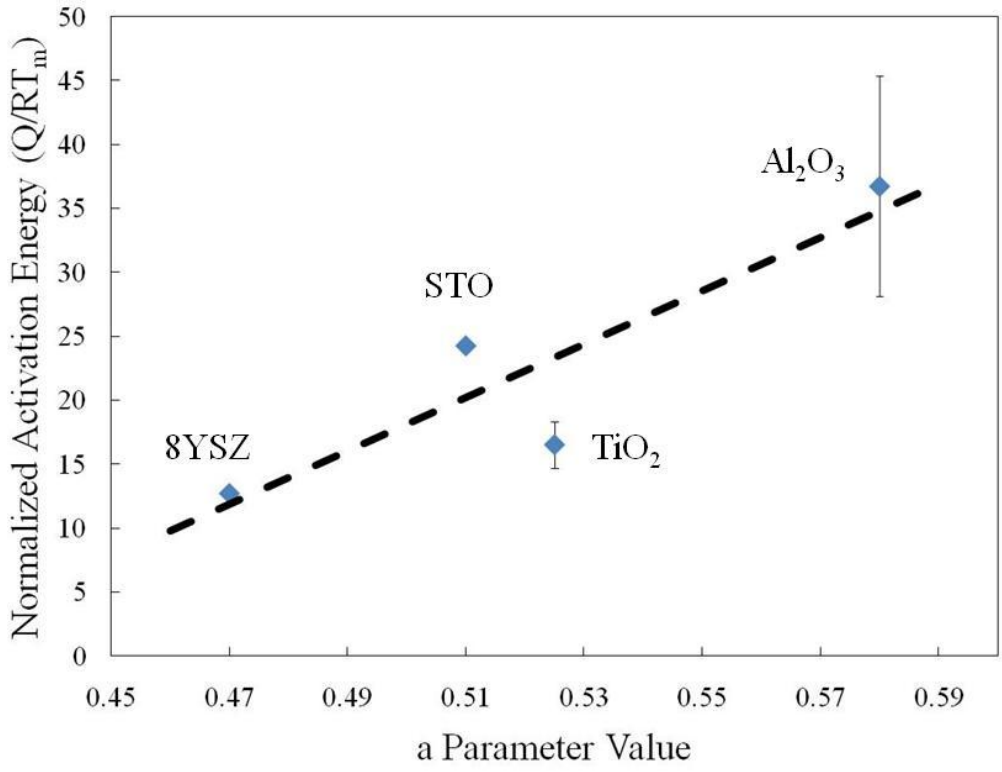

Figure 3.6: Plot of activation energy for diffusion normalized by melting temperature versus *a* parameter for all four materials. The dashed line represents the linear fit of the data.

3.5.B - Application of Model

One of the strengths of this model is that only two parameters are required for use, and that these parameters have a physical meaning. It was shown previously that the presented model is capable of fitting known CAPAD data to a sigmoidal curve. Another use for this model is in the estimation of the outcome of an experiment. A common scenario in the CAPAD community is that workers get a limited supply of an exotic oxide powder which has never been used in the CAPAD before. In this situation, the temperature required to reach full density is often not known. The model presented in this

study would apply well to this situation. When no prior data is available, it is necessary to estimate the parameters for the model.

A flow chart of the steps necessary to use the model in this situation is presented in Figure 3.7. First, the CAPAD worker should begin by preparing their sample and measuring their ρ_0. Next, the activation energy for diffusion should be acquired. From here the *a* parameter can be estimated by comparing the *a* value from literature with the *a* values listed in this work. Then, using the known *a* and ρ_0, along with *s*=6, the density-temperature relationship for the new material should be constructed using the model presented here. An *s* parameter of 6 is used because this is a commonly occurring *s* value, appearing in both 8YSZ and Al_2O_3. Both of these materials belong to different bond types and both have very different normalized activation energies for diffusion. As shown earlier, the *s* parameter is more forgiving than the *a* parameter as the maximum error is within an acceptable range (assuming that <10% error is desired). After acquiring the density-temperature relationship for the material system in question, the CAPAD workers can then process the sample to the desired density. If more samples are required, the workers can use the raw data from the first experiment to refine the model.

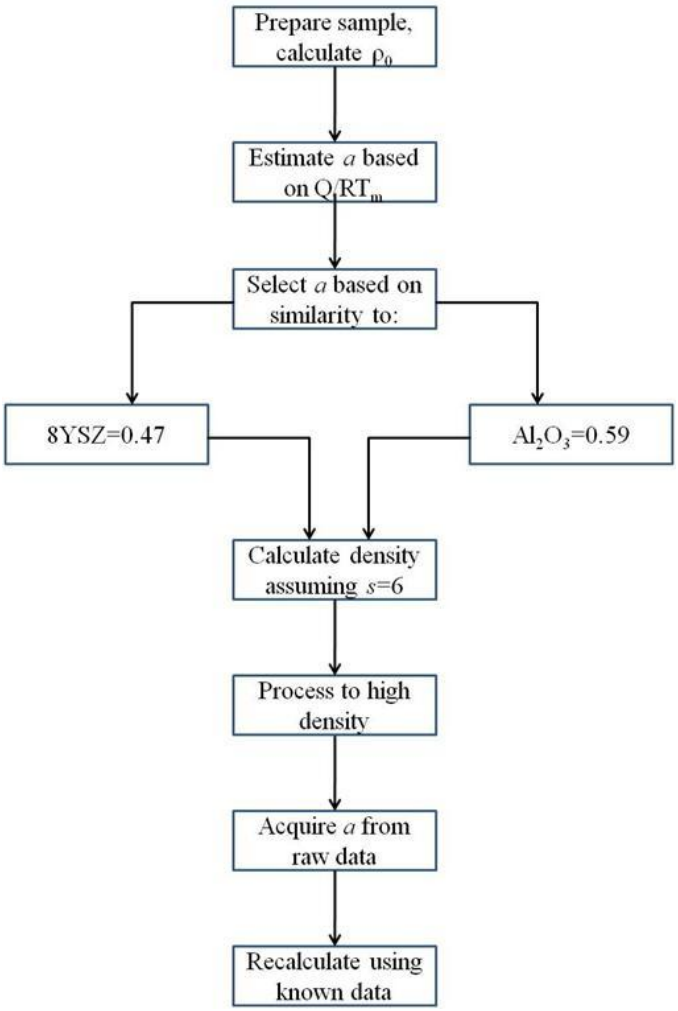

Figure 3.7: Flow chart of the recommended steps to take when using the model to assist in processing a new material system.

3.6 - Conclusion

A model of the density-temperature relationship for oxide materials processed using the CAPAD technique was constructed. This model uses two parameters, *a* and *s*, that have real physical meaning and can be found by using real data. By calculating the two parameters for multiple material systems, it was shown that every material has a unique set of model parameters that correspond to that material system's properties as

well as its associated processing conditions. Through error analysis it was found that the *a* parameter has a greater effect on the outcome of the model than the *s* parameter does. The *a* parameter is possible to estimate because it has a fundamental connection to a material's activation energy for diffusion. By following guidelines listed in this work, CAPAD workers can more accurately estimate the density-temperature relationship for material system, thus saving valuable time and resources.

References

[1] W.D. Kingery, "Sintering from Prehistoric Times to the Present," *Solid State Phenomena*, vol. 25-26, 1992, pp. 1-10.

[2] D.M. Hulbert, A. Anders, D.V. Dudina, J. Andersson, D. Jiang, C. Unuvar, U. Anselmi-Tamburini, E.J. Lavernia, and A.K. Mukherjee, "The absence of plasma in 'spark plasma sintering'," *Journal of Applied Physics*, vol. 104, 2008, p. 033305.

[3] J.E. Garay, U. Anselmi-Tamburini, and Z.A. Munir, "Enhanced growth of intermetallic phases in the Ni-Ti system by current effects," *Acta Materialia*, vol. 51, Sep. 2003, pp. 4487-4495.

[4] R. Orrù, R. Licheri, A.M. Locci, A. Cincotti, and G. Cao, "Consolidation/synthesis of materials by electric current activated/assisted sintering," *Materials Science and Engineering: R: Reports*, vol. 63, Feb. 2009, pp. 127-287.

[5] M. Meyers, A. Mishra, and D. Benson, "Mechanical properties of nanocrystalline materials," *Progress in Materials Science*, vol. 51, 2006, pp. 427-556.

[6] J.R. Morales, J.E. Garay, M. Biasini, and W.P. Beyermann, "Magnetic characterization of bulk nanostructured iron oxides," *Applied Physics Letters*, vol. 93, 2008, p. 022511.

[7] T. Hungría, J. Galy, and A. Castro, "Spark Plasma Sintering as a Useful Technique to the Nanostructuration of Piezo-Ferroelectric Materials," *Advanced Engineering Materials*, vol. 11, 2009, pp. 615-631.

[8] S.R. Casolco, J. Xu, and J.E. Garay, "Transparent/translucent polycrystalline nanostructured yttria stabilized zirconia with varying colors," *Scripta Materialia*, vol. 58, 2008, pp. 516-519.

[9] J. Xu, S.R. Casolco, and J.E. Garay, "Effect of Varying Displacement Rates on the Densification of Nanostructured Zirconia by Current Activation," *Journal of the American Ceramic Society*, vol. 92, Jul. 2009, pp. 1506-1513.

[10] E.A. Olevsky, S. Kandukuri, and L. Froyen, "Consolidation enhancement in spark-plasma sintering: Impact of high heating rates," *Journal of Applied Physics*, vol. 102, 2007, p. 114913.

[11] Y. Zhou, K. Hirao, Y. Yamauchi, and S. Kanzaki, "Densification and grain growth in pulse electric current sintering of alumina," *Journal of the European Ceramic Society*, vol. 24, 2004, pp. 3465-3470.

[12] Z. Shen, M. Johnsson, Z. Zhao, and M. Nygren, "Spark plasma sintering of alumina," *Journal of the American Ceramic Society*, vol. 85, 2002, pp. 1921-1927.

[13] J. Langer, M.J. Hoffmann, and O. Guillon, "Direct comparison between hot pressing and electric field-assisted sintering of submicron alumina," *Acta Materialia*, vol. 57, Oct. 2009, pp. 5454-5465.

[14] J.E. Garay, "Current-Activated, Pressure-Assisted Densification of Materials," *Annual Review of Materials Research*, vol. 40, Jul. 2010, pp. 445-468.

[15] P. Blöchl, E. Smargiassi, R. Car, D. Laks, W. Andreoni, and S. Pantelides, "First-principles calculations of self-diffusion constants in silicon," *Physical Review Letters*, vol. 70, Apr. 1993, pp. 2435-2438.

[16] A. Chokshi, "Diffusion, diffusion creep and grain growth characteristics of nanocrystalline and fine-grained monoclinic, tetragonal and cubic zirconia," *Scripta Materialia*, vol. 48, 2003, pp. 791-796.

[17] F.A. Mohamed and T.G. Langdon, "Deformation mechanism maps based on grain size," *Metallurgical Transactions*, vol. 5, Nov. 1974, pp. 2339-2345.

[18] X. Wang, S. Casolco, G. Xu, and J. Garay, "Finite element modeling of electric current-activated sintering: The effect of coupled electrical potential, temperature and stress," *Acta Materialia*, vol. 55, 2007, pp. 3611-3622.

[19] A. Antonelli and J. Bernholc, "Pressure effects on self-diffusion in silicon," *Physical Review B*, vol. 40, Nov. 1989, pp. 10643-10646.

[20] P. Shewmon, *Diffusion In Solids*, Warrendale, Pa: Minerals, Metals & Materials Society, 1989.

[21] J.M. Fairfield and B.J. Masters, "Self-Diffusion in Intrinsic and Extrinsic Silicon," *Journal of Applied Physics*, vol. 38, 1967, p. 3148.

[22] M.F. Ashby, "A first report on deformation-mechanism maps," *Acta Metallurgica*, vol. 20, Jul. 1972, pp. 887-897.

[23] R.L. Coble, "Sintering Crystalline Solids. I. Intermediate and Final State Diffusion Models," *Journal of Applied Physics*, vol. 32, 1961, p. 787.

[24] R.L. Coble, “Diffusion Models for Hot Pressing with Surface Energy and Pressure Effects as Driving Forces,” *Journal of Applied Physics*, vol. 41, 1970, p. 4798.

[25] M. Ashby, “A first report on sintering diagrams,” *Acta Metallurgica*, vol. 22, Mar. 1974, pp. 275-289.

[26] H. Su and D.L. Johnson, “Master Sintering Curve: A Practical Approach to Sintering,” *Journal of the American Ceramic Society*, vol. 79, Dec. 1996, pp. 3211-3217.

[27] E.A. Olevsky and L. Froyen, “Impact of Thermal Diffusion on Densification During SPS,” *Journal of the American Ceramic Society*, vol. 92, Jan. 2009, p. S122-S132.

[28] G. Maizza, S. Grasso, and Y. Sakka, “Moving finite-element mesh model for aiding spark plasma sintering in current control mode of pure ultrafine WC powder,” *Journal of Materials Science*, vol. 44, Feb. 2009, pp. 1219-1236.

[29] O. Guillon and J. Langer, “Master sintering curve applied to the Field-Assisted Sintering Technique,” *Journal of Materials Science*, vol. 45, May. 2010, pp. 5191-5195.

[30] A. Tacca, U. Anselmi-Tamburini, J.E. Garay, Z. a Munir, F. Maglia, and G. Spinolo, “Spark plasma sintering and characterization of bulk nanostructured fully stabilized zirconia: Part I. Densification studies,” *Journal of Materials Research*, vol. 19, 2004, pp. 3255-3262.

[31] A. Heuer, “Oxygen and aluminum diffusion in α-Al2O3: How much do we really understand?,” *Journal of the European Ceramic Society*, vol. 28, 2008, pp. 1495-1507.

[32] T. Seto, M. Shimada, and K. Okuyama, “Evaluation Of Sintering Of Nanometer-Sized Titania Using Aerosol Method,” *Aerosol Science Technology*, vol. 23, 1995, pp. 183-200.

[33] W.H. RHODES and W.D. KINGERY, “Dislocation Dependence of Cationic Diffusion in SrTiO3,” *Journal of the American Ceramic Society*, vol. 49, 1966, pp. 521-526.

[34] P. Angerer, “Spark-plasma-sintering (SPS) of nanostructured and submicron titanium oxide powders,” *Materials Science and Engineering A*, vol. 381, Sep. 2004, pp. 16-19.